Publ. Astron. Soc. Japan (2019) 71 (3), 54 (1–11)
doi: 10.1093/pasj/psz030
Advance Access Publication Date: 2019 April 15

Systematic study for gas-to-dust ratio of short gamma-ray burst afterglows

Kazuki Yoshida,*† **Daisuke Yonetoku**,* **Makoto Arimoto**, **Tatsuya Sawano**, **and Yasuaki Kagawa**†

Faculty of Mathmatics and Physics, Kanazawa University, Kakuma-machi, Kanazawa, Ishikawa 920-1192, Japan

*E-mail: yoshida@astro.s.kanazawa-u.ac.jp, yonetoku@astro.s.kanazawa-u.ac.jp

†JSPS Research Fellow

Received 2018 December 29; Accepted 2019 February 20

Abstract

Extragalactic X-ray absorption and optical extinction are often found in gamma-ray burst (GRB) afterglows, and they could be tracers of both circumburst and host galaxy environments. By performing spectral analyses of the spectral energy distribution of nine short GRB (SGRB) afterglows with a known redshift, we investigated the ratio of the equivalent hydrogen column density to the dust extinction, $N_{\rm H}^{\rm rest}/A_V^{\rm rest}$, in the rest frame of each SGRB. We found that the distribution of $N_{\rm H}^{\rm rest}/A_V^{\rm rest}$ is systematically smaller than for long GRBs, and is roughly consistent with the gas-to-dust ratio in the Milky Way. This result means that the measured gas-to-dust ratio of SGRBs would originate from the interstellar medium in each host galaxy. This scenario supports the prediction that SGRBs occur in non-star-forming regions in the host galaxies.

Key words: dust, extinction — galaxies: ISM — gamma-ray burst: general

1 Introduction

Gamma-ray bursts (GRBs) are grouped into two classes based on their observed duration and the spectral hardness of prompt emissions. Long GRBs (LGRBs) and short GRBs (SGRBs) typically have durations of longer than and shorter than about 2 s, respectively, and relatively softer and harder spectra, respectively (e.g., Kouveliotou et al. 1993; Lien et al. 2016). LGRBs are almost always found in star-forming regions within star-forming galaxies (Bloom et al. 2002; Fruchter et al. 2006; Sevensson et al. 2010), and their progenitors have been confirmed as the deaths of massive stars (e.g., Hjorth et al. 2003; Woosley & Bloom 2006; Kumar & Zhang 2015, and references therein). On the other hand, some fractions of SGRBs occur in elliptical galaxies showing no star formation (Fong et al. 2013; Fong & Berger 2013). Progenitors of SGRBs are considered to be the coalescence of binary neutron stars (NSs) and/or black hole (BH)–NS binaries (e.g., Eichler et al. 1989; Narayan et al. 1992). In fact, the binary NS merger event GW 170817 was observed through gravitational waves by the LIGO and Virgo collaboration, and it accompanied the SGRB candidate GRB 170817A (Abbott et al. 2017; Goldstein et al. 2017; Savchenko et al. 2017). Since a binary system should move away from its birth site until its merging by natal kicks in the compact binary merger scenario (e.g., Narayan et al. 1992; Bloom et al. 1999; Fryer et al. 1999; Belczynski et al. 2006), SGRBs may occur in non-star-forming regions inside or outside host galaxies. Therefore, investigating the surrounding environment of SGRBs and comparing it with that of LGRBs are a crucial way to interpret the SGRB's progenitor.

Studying spectral energy distributions (SEDs) of GRB afterglows is the major approach to interpreting the surrounding environments of GRBs. GRB afterglows are thought to originate from relativistically expanding jets that form shocks between the jet and the surrounding medium (e.g., Rees & Mészáros 1992, 1998), and their SEDs in the optical to X-ray band can be described by a single or broken power-law function (Sari et al. 1998; Granot & Sari 2002). Performing spectral analysis for them, we can study extinction curves following SEDs and measure the amounts of X-ray absorption and optical extinction in the host galaxy, which are usually defined as an equivalent hydrogen column density ($N_{\rm H}$) under the assumption of solar abundance and extinction in the V band (A_V), respectively. The extinction curve shows the dependence of dust attenuation on wavelength, which originates from the dust size and chemical properties, and is different for galaxies, e.g., the Milky Way (MW), the Large Magellanic Cloud (LMC), and the Small Magellanic Cloud (SMC; Pei e.g., 1992). The $N_{\rm H}/A_V$ ratio, called the gas-to-dust ratio,[1] reflects the properties of the interstellar medium (ISM) in the galaxies and is considered to vary with galaxies, e.g., the MW, LMC, and SMC (Welty et al. 2012).

According to previous studies for afterglows of LGRBs (e.g., Schady et al. 2007, 2010; Covino et al. 2013), in the optical and near-infrared (NIR) bands the extinction curve of the SMC is well fitted to SEDs of observation data, rather than that of the MW or LMC is, in almost all events. However, in the rest frame of each GRB, the ratio of hydrogen equivalent column density measured in the X-ray band to the dust extinction measured in the optical/NIR band ($N_{\rm H}^{\rm rest}/A_V^{\rm rest}$) is significantly larger than in the SMC as well as in the MW and LMC. Dust destruction caused by the intense GRB emission is discussed as a major interpretation of the large $N_{\rm H}^{\rm rest}/A_V^{\rm rest}$, but observational evidence for this has not been found (Waxman & Draine 2000; Galama & Wijers 2001; Savaglio et al. 2003; Schady et al. 2010). Schady et al. (2010) reported on the possibility that the $N_{\rm H}/A_V$ ratio of LGRBs in low-metallicity galaxies is large. On the other hand, Zafar et al. (2011) investigated the $N_{\rm H}^{\rm rest}/A_V^{\rm rest}$ ratio including the metallicity of each LGRB in detail, but they concluded that the metallicity alone cannot explain the observed high $N_{\rm H}^{\rm rest}/A_V^{\rm rest}$ ratio. Until now, a unified picture to explain such a large $N_{\rm H}^{\rm rest}/A_V^{\rm rest}$ ratio has not been established.

In this paper we systematically performed SED fitting for nine SGRBs with a known redshift using both X-ray and optical/NIR afterglow data, and investigated the ratio of equivalent hydrogen column density to optical extinction of each GRB. Furthermore, we compared this ratio with the results of LGRBs and also typical galaxy environments. The error and upper/lower limits of all fitting parameters are shown at 68% and 90% confidence levels, respectively.

[1] This is sometimes called the metal-to-dust ratio, especially when the equivalent hydrogen column density is derived from the X-ray absorption, because the dominant X-ray absorbers are strictly metallic elements.

Table 1. Samples of SGRBs.

GRB	z	$N_{\rm H}^{\rm gal}$ (10^{20} cm^{-2})	$A_V^{\rm gal}$ (mag)	Epoch (s)
050724	0.258	27.7	1.61	41783
051221A	0.5465	7.52	0.18	184701
070724A	0.457	1.21	0.04	10872
090510	0.903	1.77	0.05	28267
130603B	0.3564	2.1	0.06	52714
140903A	0.351	3.26	0.09	47117
150423A	1.394	1.77	0.08	15300
150424A	0.3	6.02	0.16	57903
170428A	0.454	6.95	0.16	3660

2 Data reduction and analysis

We used SGRBs with known redshifts observed by the X-ray Telescope (XRT) on board the Neil Gehrels Swift Observatory (Swift; Gehrels et al. 2004; Burrows et al. 2005). In addition to obvious SGRBs with $T_{90} < 2$ s, we included possible SGRB candidates with $T_{90} > 2$ s, which are considered as SGRBs with an extended soft X-ray emission following prompt emissions. Here, T_{90} is the time duration that includes 90% of the observed photon counts except for the first and the last 5% in the GRB emission observed by Swift/BAT. We selected the brightest nine SGRBs, listed in table 1, whose host galaxies were much dimmer than the optical/NIR afterglows.

Since the spectral parameters of the power-law index and the dust extinction in the SEDs of GRB afterglows are degenerate, we cannot correctly measure the dust extinction in the rest frame of SGRBs with only optical/NIR data, which are limited data points. Therefore, in order to obtain reliable spectral parameters, we performed simultaneous spectral analysis for broadband SEDs consisting of both optical/NIR and X-ray data, i.e., we estimated the spectral index in the optical/NIR band including X-ray data. In Covino et al. (2013), the optical extinctions derived from only optical/NIR data analysis were consistent with those derived from the X-ray prior analysis, as we mentioned.

2.1 Optical/NIR data

We gathered available data (not including upper limits) of optical/NIR afterglow observations from published papers and GCN Circulars,[2] and converted their magnitudes to

[2] ⟨https://gcn.gsfc.nasa.gov/⟩.

flux densities. The data we used and their references are listed in table 4 in the appendix. Using the database in the NASA/IPAC Infrared Science Archive[3] (Schlafly & Finkbeiner 2011), we converted the observed flux density of each burst to the one before affecting the galactic extinction.

Since the GRB afterglow shows power-law decline in time (Sari et al. 1998; Granot & Sari 2002), it is necessary to collect data as close as possible in time in order to create an accurate SED. Here, we ignore the time difference between each band data observed almost at the same time (or at slightly different times) when the relative uncertainty of the measured flux density ($\Delta F/F$) and the observation time ($\Delta t/t$) satisfies $\Delta F/F > \Delta t/t$. Since six of the nine samples satisfied the condition, we used the observation data of that epoch as the SEDs for these events. For the other three samples, GRB 070724A, 090510, and 140903A, we adopted a power-law function of $F(t) \propto (t - t_0)^{\alpha_{\rm opt}}$ to the observed light curve in the same band, and we estimated the flux density at the time when the interpolation and extrapolation in all bands were minimized. Here, t_0 is the trigger time and $\alpha_{\rm opt}$ is the temporal index in the optical/NIR band. The time we set for each sample is summarized in table 1.

2.2 X-ray data

X-ray observation data of SGRBs were taken from the UK Swift Science Data Centre.[4] XRT observation is generally performed in two modes: windowed timing (WT) mode and photon counting (PC) mode. The PC mode data were used as data of afterglows in this analysis, since the extended emission, whose origin is different from that of afterglows, is often observed in the WT mode (e.g., Norris & Bonnell 2006; Kagawa et al. 2015; Kisaka et al. 2017). The light-curve data were taken from the XRT light curve repository[5] (Evans et al. 2007, 2009). We extracted source and background event data from circular regions of 20 and 40 pixels in radius (corresponding to 47″ and 94″), respectively, which are circular regions recommended in the Swift XRT User Guide Version 1.2.[6] Using `XSELECT` software (v2.4),[7] we extracted spectral data from the cleaned event data. For the spectral analysis, ancillary response files were created by `xrtmkarf` (v0.6.3) and response matrices were taken from the calibration database files.[8]

Y. Kagawa et al. (in preparation) analyze time-resolved X-ray spectra whose time intervals were divided such that each spectrum contained 128 photons, and the spectral parameters at each observed time were obtained. They also analyzed the time-averaged spectra with all observation data in PC mode, and confirmed that the photon indices of both results were consistent with each other within the error. Thus we performed time-averaged spectral analyses with the entire PC mode data to maximize the signal-to-noise ratio. The time-averaged spectra were grouped into 20 counts per energy bin.

In order to determine the X-ray flux at any given time, we adopted a power-law function with the temporal index of the X-ray band ($\alpha_{\rm X}$) for the X-ray light curves in the same way as we did for optical/NIR light curves, where light curve data were taken from the Swift-XRT light curve repository,[9] in which a systematic search for temporal breaks had been performed for light curves (Evans et al. 2007, 2009). Considering their results and excluding the time at the temporal breaks, we defined fitting intervals with simple power-laws. The fitting results are shown in figure 1 as red solid lines. Using the best-fitting result, we estimated a conversion factor from average flux to that at the focusing time and renormalized the time-averaged X-ray spectra for the broadband SED analysis.

2.3 Spectral analysis

The spectral analysis was carried out with the `XSPEC` software (v12.9.0)[10] and the model fit prepared therein. Based on a standard synchrotron shock model (Sari et al. 1998; Granot & Sari 2002), we adopted a `powerlaw` model and a `bknpower` model for the broadband SEDs. The X-ray spectral index ($\beta_{\rm X}$) was derived from the photon index (Γ) of the power law in the relation $\beta_{\rm X} = 1 - \Gamma$. Then we imposed the spectral index of the optical/NIR region, $\beta_{\rm opt} = \beta_{\rm X}$ in the `powerlaw` model and $\beta_{\rm opt} = \beta_{\rm X} - 0.5$ in the `bknpower` model. The latter case corresponds to the condition where the cooling frequency of the synchrotron emission is located between the optical/NIR and X-ray ranges (Sari et al. 1998; Granot & Sari 2002).

We added `phabs` and `zphabs` models corresponding to the photo-electric absorptions in our Galaxy and host galaxy, respectively. The parameter of the Galactic equivalent hydrogen column density ($N_{\rm H}^{\rm gal}$) was fixed at the amount calculated for the sky coordinates of each SGRB by the UK Swift Science Data Center database[11] (Willingale et al. 2013), as shown in table 1. The equivalent hydrogen column density in the host galaxy ($N_{\rm H}^{\rm rest}$) was derived from the model fit where solar abundances were assumed. We

[3] ⟨https://irsa.ipac.caltech.edu/applications/DUST/⟩.
[4] ⟨http://www.swift.ac.uk/index.php⟩.
[5] ⟨http://www.swift.ac.uk/xrt_curves/⟩.
[6] ⟨https://swift.gsfc.nasa.gov/analysis/⟩.
[7] ⟨https://heasarc.gsfc.nasa.gov/docs/software/lheasoft/ftools/xselect/⟩.
[8] ⟨https://heasarc.gsfc.nasa.gov/docs/heasarc/caldb/swift/⟩.
[9] ⟨http://www.swift.ac.uk/xrt_curves/⟩.
[10] ⟨https://heasarc.gsfc.nasa.gov/xanadu/xspec/⟩.
[11] ⟨http://www.swift.ac.uk/analysis/nhtot/index.php⟩.

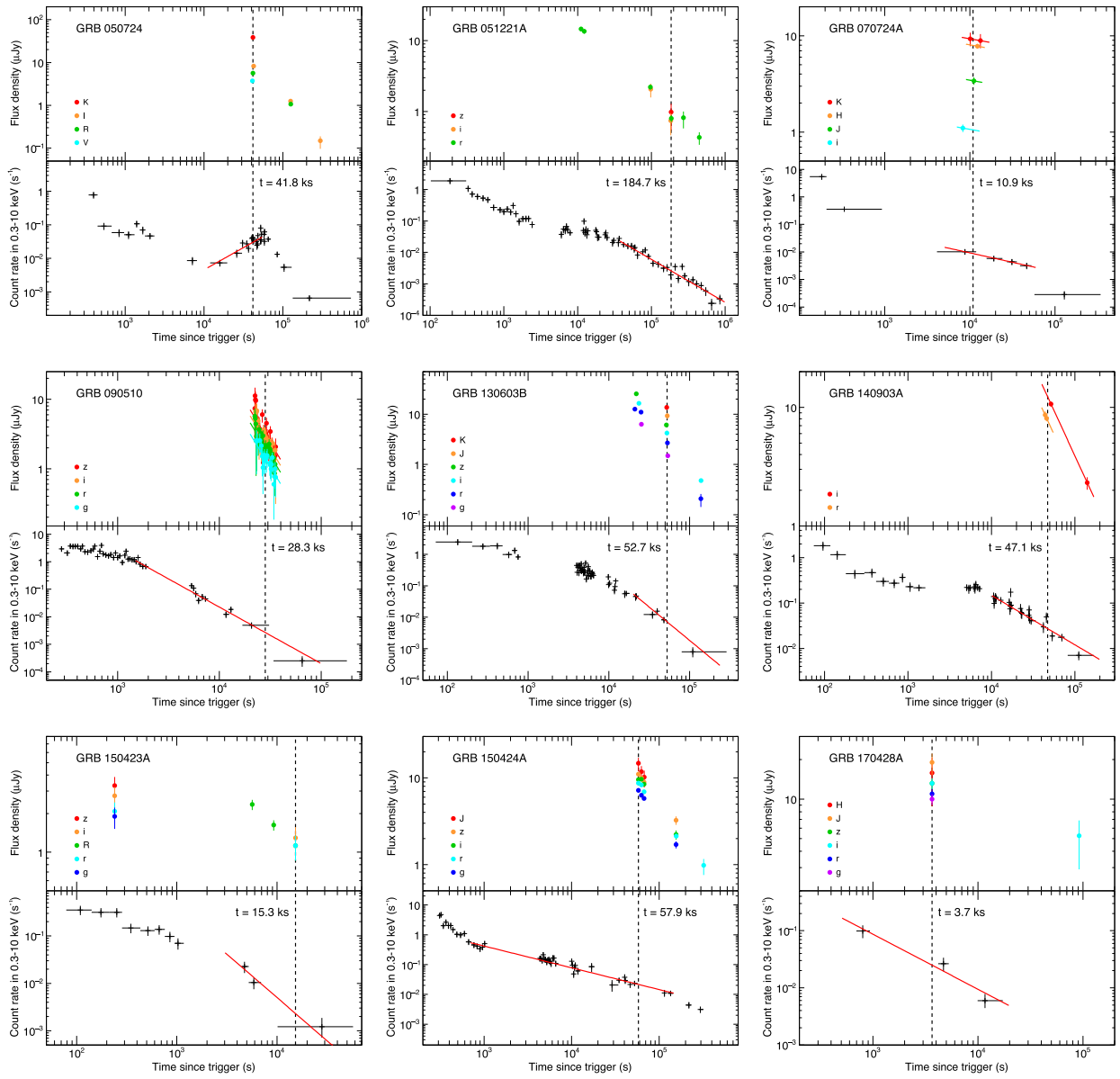

Fig. 1. Optical/NIR and X-ray light curves in the observer frame. The solid lines and the vertical dashed lines show the best-fit power-law models of each observation band and the epoch of broadband SEDs of each SGRB, respectively. (Color online)

note that metallicities of the SGRB host galaxies showed a wide range of values, but on average it is about a solar abundances (Berger 2014, and references therein).

To compute the extinction in the host galaxy, we used the `zdust` model that considered wavelength extinction by dust grains as described by Pei (1992). There are three major models of the extinction curves in the MW, LMC, and SMC environments. We adopted all three extinction models and investigated the differences in extinction in each model. All the results of our spectral analysis are summarized in table 5, but in section 3 we reported on the results of using the MW extinction model because there is little difference in the amount of optical extinction between the three models. In fact, the three extinction models are almost the same within the wavelength range of the observation data in the rest frame of nine SGRBs.

3 Results

Figure 1 shows the optical/NIR and X-ray light curves and the epoch of the broadband SED of each GRB. Although the time when the multi-band observation was performed for GRB 050724 is in the X-ray flare phase, we set this epoch for the broadband SED because it is reported by Berger et al. (2005) (see also Malesani et al. 2007), that the optical/NIR and X-ray emissions might belong to the same

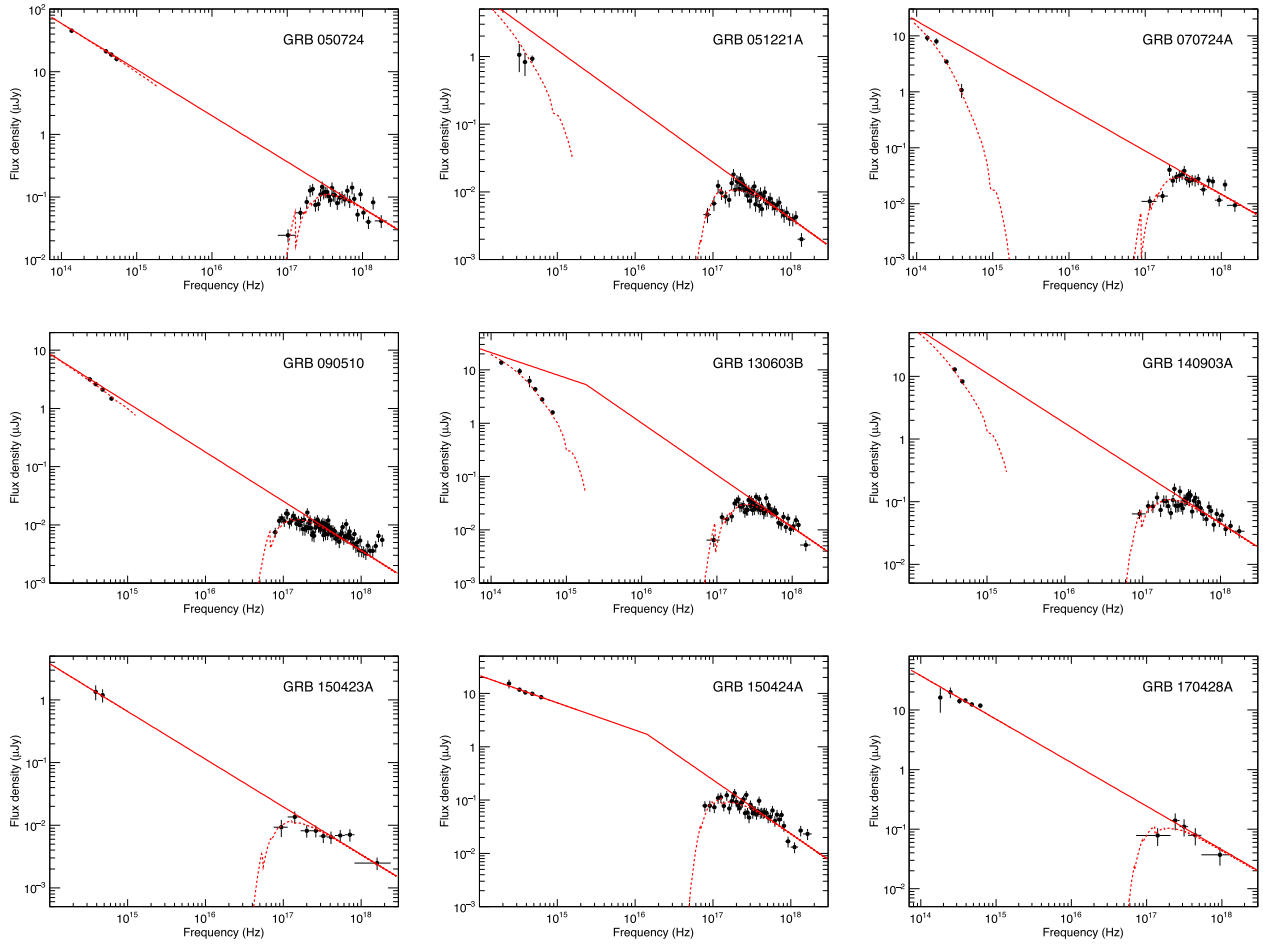

Fig. 2. Spectral energy distributions of nine SGRBs. The optical/NIR data points are corrected for Galactic extinction, but the X-ray data points are not corrected for Galactic absorption. The solid lines show the best-fit unabsorbed spectral model corrected for absorption and extinction. The dashed lines show the best-fit absorbed model including the Galactic and host-galactic absorption, and host-galactic extinction. (Color online)

Table 2. Results of spectral analysis.

GRB	$N_{\rm H}^{\rm rest}$ (10^{21} cm^{-2})	$A_V^{\rm rest}$ (mag)	$\beta_{\rm X}$	$E_{\rm bk}$ (eV)	χ^2 (dof)	Null hypothesis probability
050724	<0.21	<0.12	$-0.74^{+0.01}_{-0.01}$	—	40 (31)	0.121
051221A	$0.56^{+0.31}_{-0.29}$	$0.81^{+0.37}_{-0.36}$	$-0.83^{+0.06}_{-0.06}$	—	44 (46)	0.544
070724A	$4.03^{+0.73}_{-0.63}$	$1.89^{+0.31}_{-0.30}$	$-0.77^{+0.02}_{-0.02}$	—	23 (19)	0.226
090510	$1.53^{+0.28}_{-0.26}$	$0.07^{+0.07}_{-0.07}$	$-0.84^{+0.02}_{-0.02}$	—	107 (85)	0.051
130603B	$2.99^{+0.30}_{-0.36}$	$1.14^{+0.10}_{-0.10}$	$-0.98^{+0.08}_{-0.07}$	8^{+19}_{-6}	48 (49)	0.498
140903A	$1.53^{+0.31}_{-0.28}$	$0.79^{+0.23}_{-0.24}$	$-0.80^{+0.03}_{-0.03}$	—	49 (39)	0.128
150423A	$1.59^{+1.50}_{-1.17}$	<0.55	$-0.76^{+0.03}_{-0.03}$	—	6 (7)	0.536
150424A	$0.32^{+0.23}_{-0.22}$	<0.15	$-1.01^{+0.07}_{-0.07}$	59^{+82}_{-34}	66 (46)	0.027
170428A	<2.55	<0.09	$-0.73^{+0.03}_{-0.02}$	—	8 (7)	0.344

component. In GRB 150423A, there are two times with multi-band observation data, i.e., an early epoch (∼240 s) and a later one (∼15300 s). Since the extended emission was observed in the early epoch (Kisaka et al. 2017; Y. Kagawa in preparation), we selected the later epoch.

The broadband SEDs with best-fit models are shown in figure 2, and the results of our spectral analyses are summarized in table 2 (see also table 5 in the appendix). For the SEDs of two SGRBs (GRB 130603B, 150424A), the broken power-law models have better fitting results than

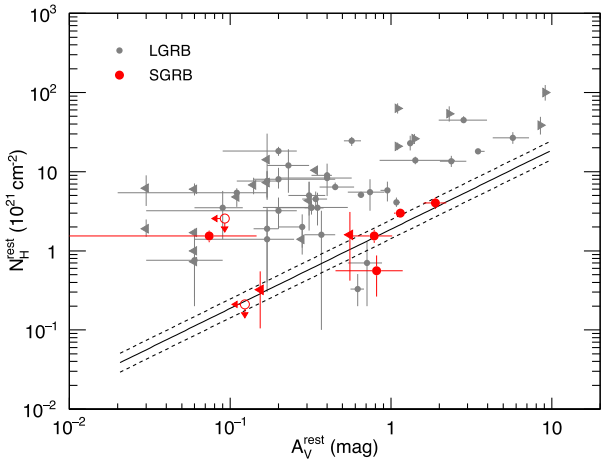

Fig. 3. Rest-frame column density versus rest-frame extinction. The red and gray points are our results in this paper and those of LGRBs by Covino et al. (2013). The triangles are the upper limits at the 90% confidence level. The solid and dashed lines show the typical gas-to-dust ratio for the Milky Way and the corresponding 1σ uncertainty (Welty et al. 2012). (Color online)

the single power-law model. These are consistent with previous studies (de Ugarte Postigo et al. 2014; Knust et al. 2017).

Figure 3 shows a scatter plot between N_H^{rest} and A_V^{rest} of SGRBs (this work) and LGRBs (Covino et al. 2013), and the typical gas-to-dust ratio of the MW, $N_H/A_V = 1.9 \times 10^{21}$ cm^{-2} mag^{-1} (Welty et al. 2012). As shown in figure 3, we found that the N_H^{rest}/A_V^{rest} ratio in the rest frame of an SGRB is systematically smaller than that of an LGRB, and is roughly consistent with the gas-to-dust ratio in the MW.

4 Discussion

In order to investigate the selection effect on N_H^{rest}, we analyzed X-ray afterglow spectra of all 20 SGRBs (not including our nine samples) with a known redshift observed by Swift/XRT before the end of 2017, which did not have any nearly simultaneous optical/NIR data. We performed the spectral analysis for each time-averaged spectrum consisting of observation data in PC mode. The sample and the fitting results are listed in table 3. Figure 4 shows histograms of the best-fit value of N_H^{rest} for our initial nine samples and the additional 20 samples. We created a cumulative distribution of the best-fit N_H^{rest} and applied the Kolmogorov–Smirnov test to it. Then, we found the null hypothesis probability of 0.79, and our nine samples show the same N_H^{rest} distribution as the other 20 SGRBs. Therefore we concluded that the N_H^{rest} of our nine SGRBs were not affected by the selection bias, while we cannot give further arguments on the selection bias in A_V^{rest} under the limited observation data. Since Krühler et al. (2011) reported on an anti-correlation between A_V^{rest} and the N_H^{rest}/A_V^{rest} ratio for LGRBs, the selection bias in A_V^{rest} should be discussed in detail based on future SGRB observation data.

In our nine SGRB sample, the measured gas-to-dust ratio of SGRBs was fairly close to that of the MW. Our result means that a major contribution of both the extinction in the optical/NIR band and the absorption in the X-ray band originates from the ISM in the host galaxy of the SGRB. In other words, most SGRBs are likely to occur not in star-forming regions but in typical ISM environments of galaxies

Table 3. Samples of the additional 20 SGRBs.

GRB	z	N_H^{gal} (10^{20} cm^{-2})	N_H^{rest} (10^{21} cm^{-2})
060614	0.125	2.09	$0.11^{-0.01}_{-0.01}$
060801	1.131	1.45	<1.4
061006	0.4377	25.1	<2.3
061201	0.111	6.8	<0.32
070714B	0.923	9.82	$0.87^{+0.62}_{-0.57}$
070809	0.2187	8.62	<1.1
071227	0.383	1.31	<3.0
080123	0.495	2.52	<1.7
080905	0.121	13.5	$1.28^{+0.91}_{-0.77}$
090426	2.609	1.58	<3.0
090530	1.266	1.84	$2.20^{+0.81}_{-0.76}$
100117A	0.915	2.97	$1.11^{+1.13}_{-0.97}$
100625A	0.453	2.23	<0.66
100816A	0.804	5.70	$1.24^{+0.63}_{-0.57}$
101219A	0.718	5.91	$4.39^{+3.69}_{-3.35}$
111117A	2.211	4.12	$17.5^{+9.8}_{-8.1}$
160228A	1.64	8.98	<11
160410A	1.717	1.8	<11
160624A	0.483	9.31	<17
160821B	0.16	5.95	<0.53

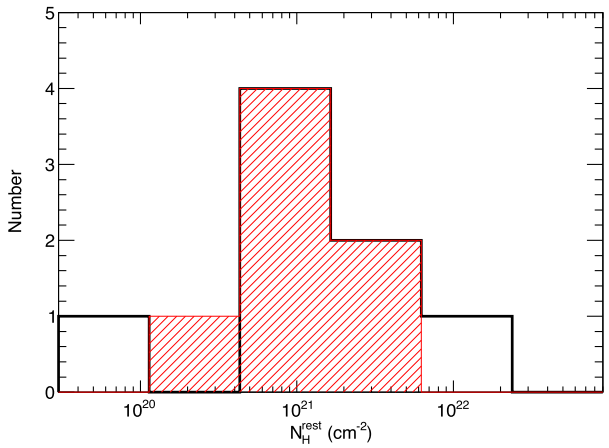

Fig. 4. Histgrams of the equivalent hydrogen column density in the GRB rest frame. The red and black lines show the distributions of our nine SGRBs and the additional 20 SGRBs, respectively. (Color online)

such as the MW. This result on the environment is consistent with the scenario that the coalescence of compact binaries is the origin of SGRBs because the system must move away from the location of their birth by natal kicks until its merging (e.g., Narayan et al. 1992; Bloom et al. 1999; Fryer et al. 1999; Belczynski et al. 2006).

$N_{\rm H}^{\rm rest}$ will show the amount of the intervening ISM within the host galaxy. In our results, we found approximately half of SGRB samples show $N_{\rm H}^{\rm rest}$ to be consistent with zero, whereas we obtained only marginal upper limits on them. These SGRBs are considered to occur on the outskirts or outside of the host galaxies in which there is almost no X-ray absorption (and dust extinction) by the ISM. Moreover, whereas GRB 170817A with GW 170817, whose origin is a binary neutron star merger (Abbott et al. 2017; Goldstein et al. 2017; Savchenko et al. 2017) that occurred at only $1\,r_{\rm e}$ from the center of the host galaxy, $r_{\rm e}$ is given by a Sérsic model (Ciotti & Bertin 1999). However, the X-ray absorption and optical extinction in the host galaxy are not significantly detected (Levan et al. 2017; Pooley et al. 2018). This event might occur at a location apart from the host galaxy toward the observer's side. The $N_{\rm H}^{\rm rest}$ value might be an indicator of the offset along the line of sight.

Acknowledgement

We gratefully thank the anonymous referee for quick responses and helpful comments, and we also acknowledge the quick and kind responses of the editors. We also thank Yuu Niino for useful discussions. This work made use of data supplied by the UK Swift Science Data Centre at the University of Leicester, and is supported by JSPS KAKENHI Grant Numbers JP17J00905 (KY), JP16H06342 (DY), JP18J13042 (YK), MEXT KAKENHI Grant Numbers JP18H04580 (DY), JP17H06362 (MA), and the Sakigake 2018 Project of Kanazawa University (DY). MA acknowledges support from the JSPS Leading Initiative for Excellent Young Researchers program.

Appendix. Optical/NIR observation data and results of spectral analysis

We show the optical/NIR observation data with their references (table 4) and the results of spectral analysis for all model fits (table 5).

Table 4. Optical/NIR observation data of our sample.

GRB	Filter	δt^* (s)	Flux† (μJy)	Reference‡
050724	K	41760	$38.7^{+1.4}_{-1.4}$	(a)
	I	42517	$8.2^{+0.2}_{-0.2}$	(b)
		125420	$1.3^{+0.1}_{-0.1}$	(b)
		298980	$0.15^{+0.05}_{-0.04}$	(b)
	R	41797	$5.7^{+0.2}_{-0.2}$	(b)
		126160	$1.1^{+0.1}_{-0.1}$	(b)
	V	41070	$3.7^{+0.1}_{-0.1}$	(b)
051221A	z	184697	$0.98^{+0.44}_{-0.30}$	(c)
	i	97986	$2.1^{+0.5}_{-0.4}$	(c)
		183522	$0.74^{+0.28}_{-0.21}$	(c)
	r	11120	$14.6^{+1.1}_{-1.0}$	(c)
		12277	$13.6^{+1.0}_{-1.0}$	(c)
		97001	$2.2^{+0.2}_{-0.2}$	(c)
		185890	$0.80^{+0.09}_{-0.08}$	(c)
		272419	$0.82^{+0.24}_{-0.19}$	(c)
		445116	$0.43^{+0.09}_{-0.08}$	(c)
070724A§	K	10080	$9.3^{+1.5}_{-1.5}$	(d)
		13320	$8.9^{+1.5}_{-1.5}$	(d)
	H	12240	$7.8^{+0.4}_{-0.4}$	(d), (e)
	J	11160	$3.4^{+0.3}_{-0.3}$	(d), (e)
	i	8280	$1.1^{+0.1}_{-0.1}$	(d)
090510	z	22299	$7.4^{+5.0}_{-3.0}$	(f)
		22401	$11.3^{+5.0}_{-3.5}$	(f)

Table 4. (Continued)

GRB	Filter	δt^* (s)	Flux† (μJy)	Reference‡
090510	z	22609	$9.9^{+4.4}_{-3.1}$	(f)
		22743	$9.5^{+2.8}_{-2.2}$	(f)
		23639	$5.3^{+1.8}_{-1.4}$	(f)
		24093	$4.0^{+2.0}_{-1.4}$	(f)
		24984	$3.6^{+1.4}_{-1.0}$	(f)
		25889	$2.4^{+1.2}_{-0.8}$	(f)
		26335	$6.0^{+1.4}_{-1.2}$	(f)
		27234	$3.5^{+1.1}_{-0.8}$	(f)
		28125	$2.6^{+1.0}_{-0.7}$	(f)
		28569	$3.2^{+1.1}_{-0.8}$	(f)
		29024	$4.5^{+1.1}_{-0.9}$	(f)
		29475	$2.8^{+1.3}_{-0.9}$	(f)
		30375	$2.3^{+1.0}_{-0.7}$	(f)
		30831	$2.4^{+1.3}_{-0.8}$	(f)
		31725	$3.4^{+0.8}_{-0.7}$	(f)
		32628	$1.9^{+1.0}_{-0.7}$	(f)
		33077	$2.3^{+0.7}_{-0.5}$	(f)
		35270	$1.5^{+0.7}_{-0.5}$	(f)
		35715	$2.1^{+0.9}_{-0.7}$	(f)
090510	i	22609	$6.6^{+2.9}_{-2.0}$	(f)
		22931	$5.0^{+2.1}_{-1.5}$	(f)
		23127	$6.5^{+2.5}_{-1.8}$	(f)
		23313	$6.9^{+2.5}_{-1.8}$	(f)

Table 4. (Continued)

GRB	Filter	δt^* (s)	Flux† (μJy)	Reference‡
090510	*i*	23639	$4.2^{+1.4}_{-1.0}$	(f)
		24093	$4.9^{+1.0}_{-0.8}$	(f)
		24540	$2.8^{+1.4}_{-0.9}$	(f)
		24984	$3.5^{+1.3}_{-0.9}$	(f)
		25443	$2.6^{+1.1}_{-0.8}$	(f)
		25889	$2.3^{+1.1}_{-0.7}$	(f)
		26780	$2.0^{+0.6}_{-0.4}$	(f)
		27234	$3.6^{+0.7}_{-0.6}$	(f)
		27679	$3.4^{+0.6}_{-0.5}$	(f)
		28125	$2.7^{+0.7}_{-0.6}$	(f)
		28569	$2.9^{+0.8}_{-0.6}$	(f)
		29024	$2.7^{+0.7}_{-0.6}$	(f)
		29475	$2.4^{+0.7}_{-0.6}$	(f)
		29922	$2.3^{+0.8}_{-0.6}$	(f)
		30375	$2.2^{+0.7}_{-0.5}$	(f)
		30831	$2.5^{+0.8}_{-0.6}$	(f)
		31275	$1.9^{+0.4}_{-0.3}$	(f)
		31725	$2.1^{+0.4}_{-0.4}$	(f)
		32170	$1.3^{+0.6}_{-0.4}$	(f)
		32628	$2.3^{+0.7}_{-0.5}$	(f)
		33077	$1.8^{+0.6}_{-0.4}$	(f)
		33524	$2.3^{+0.3}_{-0.3}$	(f)
		34369	$1.1^{+0.7}_{-0.4}$	(f)
		35270	$1.9^{+0.6}_{-0.4}$	(f)
		35715	$1.0^{+0.7}_{-0.4}$	(f)
090510	*r*	22299	$5.7^{+2.4}_{-1.7}$	(f)
		22503	$5.3^{+2.2}_{-1.6}$	(f)
		22743	$4.4^{+1.6}_{-1.2}$	(f)
		22931	$2.5^{+1.8}_{-1}$	(f)
		23127	$2.9^{+1.8}_{-1.1}$	(f)
		23313	$2.5^{+1.6}_{-1.0}$	(f)
		24093	$2.2^{+0.7}_{-0.5}$	(f)
		24540	$3.7^{+0.7}_{-0.6}$	(f)
		24984	$2.6^{+0.9}_{-0.6}$	(f)
		25443	$3.3^{+0.8}_{-0.6}$	(f)
		25889	$2.8^{+0.7}_{-0.6}$	(f)
		26335	$2.1^{+0.7}_{-0.5}$	(f)
		26780	$3.0^{+0.7}_{-0.6}$	(f)
		27234	$2.2^{+0.6}_{-0.4}$	(f)
		27679	$1.8^{+0.4}_{-0.3}$	(f)
		28125	$1.9^{+0.5}_{-0.4}$	(f)
		28569	$2.1^{+0.5}_{-0.4}$	(f)
		29024	$1.7^{+0.6}_{-0.4}$	(f)
		29475	$2.0^{+0.5}_{-0.4}$	(f)
		29922	$1.9^{+0.5}_{-0.4}$	(f)
		30375	$2.1^{+0.4}_{-0.4}$	(f)
		30831	$2.3^{+0.5}_{-0.4}$	(f)

Table 4. (Continued)

GRB	Filter	δt^* (s)	Flux† (μJy)	Reference‡
090510	*r*	31275	$1.9^{+0.5}_{-0.4}$	(f)
		31725	$1.8^{+0.4}_{-0.3}$	(f)
		32170	$1.5^{+0.5}_{-0.3}$	(f)
		32628	$1.6^{+0.4}_{-0.3}$	(f)
		33077	$1.2^{+0.4}_{-0.3}$	(f)
		33524	$1.4^{+0.4}_{-0.3}$	(f)
		34369	$1.4^{+0.4}_{-0.3}$	(f)
		34815	$0.86^{+0.45}_{-0.30}$	(f)
		35270	$1.2^{+0.4}_{-0.3}$	(f)
090510	*g*	23127	$2.6^{+1.7}_{-1.0}$	(f)
		23639	$2.5^{+1.0}_{-0.7}$	(f)
		24984	$2.6^{+0.9}_{-0.7}$	(f)
		25889	$2.1^{+0.7}_{-0.5}$	(f)
		26335	$1.5^{+0.7}_{-0.5}$	(f)
		26780	$1.0^{+0.6}_{-0.4}$	(f)
		27234	$1.4^{+0.6}_{-0.4}$	(f)
		27679	$1.6^{+0.4}_{-0.3}$	(f)
		28125	$1.3^{+0.5}_{-0.3}$	(f)
		29024	$1.4^{+0.5}_{-0.4}$	(f)
		29475	$1.5^{+0.5}_{-0.4}$	(f)
		31275	$1.2^{+0.4}_{-0.3}$	(f)
		31725	$1.1^{+0.4}_{-0.3}$	(f)
		32170	$0.99^{+0.33}_{-0.25}$	(f)
		32628	$1.1^{+0.4}_{-0.3}$	(f)
		33077	$1.4^{+0.3}_{-0.3}$	(f)
		34369	$0.60^{+0.41}_{-0.24}$	(f)
		34815	$0.77^{+0.25}_{-0.19}$	(f)
		35270	$1.0^{+0.3}_{-0.3}$	(f)
		35715	$0.75^{+0.37}_{-0.25}$	(f)
130603B	*K*	52099	$13.7^{+1.5}_{-1.3}$	(g)
	J	53050	$9.3^{+1.3}_{-1.1}$	(g)
	z	21946	$25.4^{+1.4}_{-1.4}$	(g)
		51754	$6.1^{+0.2}_{-0.2}$	(g)
	i	23674	$16.4^{+0.9}_{-0.9}$	(g)
		52445	$4.2^{+0.1}_{-0.1}$	(g)
	r	21082	$12.6^{+0.2}_{-0.2}$	(g)
		25056	$11.0^{+0.2}_{-0.2}$	(g)
		53136	$2.7^{+0.1}_{-0.1}$	(g)
		138240	$0.21^{+0.07}_{-0.05}$	(g)
	g	25402	$6.3^{+0.4}_{-0.3}$	(g)
		53827	$1.5^{+0.1}_{-0.1}$	(g)
140903A	*i*	51840	$10.7^{+0.5}_{-0.5}$	(h)
		140832	$2.3^{+0.3}_{-0.3}$	(h)
	r	44064	$8.6^{+0.7}_{-0.6}$	(h)
		45792	$8.1^{+0.5}_{-0.4}$	(h)
150423A	*z*	240	$3.3^{+0.7}_{-0.6}$	(i)

Table 4. (Continued)

GRB	Filter	δt^* (s)	Flux† (μJy)	Reference‡
	i	240	$2.8^{+0.6}_{-0.5}$	(i)
		15300	$1.3^{+0.4}_{-0.3}$	(j)
	R	5655	$2.4^{+0.2}_{-0.2}$	(k)
		9255	$1.6^{+0.2}_{-0.1}$	(k)
	r	240	$2.1^{+0.4}_{-0.4}$	(i)
		15300	$1.1^{+0.3}_{-0.2}$	(j)
	g	240	$1.9^{+0.4}_{-0.3}$	(i)
150424A	J	57929	$14.7^{+2.8}_{-2.4}$	(l)
		62670	$11.8^{+2.3}_{-1.9}$	(l)
		67399	$10.2^{+2.4}_{-1.9}$	(l)
	z	57903	$11.1^{+0.6}_{-0.6}$	(l)
		62645	$10.0^{+0.5}_{-0.5}$	(l)
		67374	$9.0^{+0.5}_{-0.5}$	(l)
		156355	$3.3^{+0.4}_{-0.3}$	(l)
	i	57903	$9.5^{+0.5}_{-0.4}$	(l)
		62645	$9.6^{+0.4}_{-0.3}$	(l)
		67374	$8.5^{+0.4}_{-0.4}$	(l)
		156355	$2.2^{+0.3}_{-0.3}$	(l)
	r	57903	$8.7^{+0.2}_{-0.2}$	(l)
		62645	$8.3^{+0.2}_{-0.2}$	(l)
		67277	$6.9^{+0.2}_{-0.2}$	(l)

Table 4. (Continued)

GRB	Filter	δt^* (s)	Flux† (μJy)	Reference‡
150424A	r	156582	$2.1^{+0.1}_{-0.1}$	(l)
		323218	$0.98^{+0.22}_{-0.18}$	(l)
	g	57903	$7.2^{+0.3}_{-0.3}$	(l)
		62645	$6.3^{+0.2}_{-0.2}$	(l)
		67277	$5.8^{+0.2}_{-0.2}$	(l)
		156123	$1.7^{+0.2}_{-0.2}$	(l)
170428	H	3660	$15.8^{+7.1}_{-4.9}$	(m)
	J	3660	$19.1^{+3.9}_{-3.2}$	(m)
	z	3660	$13.2^{+1.3}_{-1.2}$	(m)
	i	3660	$13.2^{+1.3}_{-1.2}$	(m)
		91692	$5.2^{+2.3}_{-1.6}$	(n)
	r	3660	$11.0^{+1.1}_{-1.0}$	(m)
	g	3660	$10.0^{+1.0}_{-0.9}$	(m)

*Time since the trigger time (s).

† If not specified, the flux is not corrected for extinctions of our Galaxy or the host one in the direction of the GRB.

‡ (a) Berger et al. (2005); (b) Malesani et al. (2007); (c) Soderberg et al. (2006); (d) Berger et al. (2009); (e) Fong et al. (2015); (f) Nicuesa Guelbenzu et al. (2012); (g) de Ugarte Postigo et al. (2014); (h) Troja et al. (2016); (i) Varela, Knust, and Greiner (2015); (j) Littlejohns et al. (2015); (k) Kann et al. (2015); (l) Knust et al. (2017); (m) Bolmer, Steinle, and Schady (2017); (n) Troja et al. (2017).

§The fluxes are corrected for Galactic extinction in the direction of the GRB.

Table 5. Results of spectral analysis for all model fits.

GRB	Model	N_H^{rest} (10^{21} cm^{-2})	A_V^{rest} (mag)	β_X	E_{bk} (eV)	χ^2/(dof)	Null hypothesis probability
050724	MW/po	<0.21	<0.12	$-0.74^{+0.01}_{-0.01}$	—	40 (31)	0.121
	LMC/po	<0.21	<0.19	$-0.74^{+0.01}_{-0.01}$	—	40 (31)	0.121
	SMC/po	<0.21	<0.21	$-0.74^{+0.01}_{-0.01}$	—	40 (31)	0.121
	MW/bknpo	<0.39	$0.52^{+0.15}_{-0.15}$	$-0.87^{+0.07}_{-0.06}$	5^{+12}_{-3}	37 (30)	0.183
	LMC/bknpo	<0.39	$0.51^{+0.14}_{-0.15}$	$-0.87^{+0.07}_{-0.06}$	5^{+12}_{-3}	37 (30)	0.182
	SMC/bknpo	<0.39	$0.51^{+0.15}_{-0.15}$	$-0.87^{+0.07}_{-0.06}$	5^{+12}_{-3}	37 (30)	0.180
051221A	MW/po	$0.56^{+0.31}_{-0.29}$	$0.81^{+0.37}_{-0.36}$	$-0.83^{+0.06}_{-0.06}$	—	44 (46)	0.544
	LMC/po	$0.55^{+0.31}_{-0.29}$	$0.78^{+0.35}_{-0.35}$	$-0.83^{+0.06}_{-0.06}$	—	44 (46)	0.540
	SMC/po	$0.51^{+0.30}_{-0.29}$	$0.72^{+0.34}_{-0.34}$	$-0.82^{+0.05}_{-0.05}$	—	45 (46)	0.522
	MW/bknpo	$1.00^{+0.40}_{-0.37}$	<1.02	$-0.95^{+0.08}_{-0.08}$	68^{+153}_{-46}	38 (45)	0.743
	LMC/bknpo	$0.99^{+0.40}_{-0.23}$	<0.98	$-0.95^{+0.09}_{-0.08}$	65^{+155}_{-53}	38 (45)	0.743
	SMC/bknpo	$0.98^{+0.41}_{-0.23}$	<0.88	$-0.94^{+0.09}_{-0.08}$	64^{+157}_{-50}	38 (45)	0.743
070724A	MW/po	$4.03^{+0.73}_{-0.63}$	$1.89^{+0.31}_{-0.30}$	$-0.77^{+0.02}_{-0.02}$	—	23 (19)	0.226
	LMC/po	$4.02^{+0.73}_{-0.63}$	$1.85^{+0.31}_{-0.29}$	$-0.77^{+0.02}_{-0.02}$	—	23 (19)	0.227
	SMC/po	$4.00^{+0.73}_{-0.63}$	$1.92^{+0.33}_{-0.31}$	$-0.77^{+0.02}_{-0.02}$	—	23 (19)	0.229
	MW/bknpo	$4.54^{+1.20}_{-0.72}$	$2.55^{+0.33}_{-0.36}$	$-0.85^{+0.13}_{-0.05}$	2^{+14}_{-2}	23 (18)	0.199
	LMC/bknpo	$4.54^{+1.21}_{-0.71}$	$2.49^{+0.33}_{-0.36}$	$-0.85^{+0.13}_{-0.05}$	2^{+15}_{-2}	23 (18)	0.199
	SMC/bknpo	$4.51^{+1.26}_{-0.70}$	$2.58^{+0.33}_{-0.39}$	$-0.84^{+0.14}_{-0.08}$	2^{+17}_{-2}	23 (18)	0.196

Table 5. (Continued)

GRB	Model	N_H^{rest} (10^{21} cm^{-2})	A_V^{rest} (mag)	β_X	E_{bk} (eV)	χ^2/(dof)	Null hypothesis probability
090510	MW/po	$1.53^{+0.28}_{-0.26}$	$0.07^{+0.07}_{-0.07}$	$-0.84^{+0.02}_{-0.02}$	—	107 (85)	0.051
	LMC/po	$1.53^{+0.28}_{-0.26}$	<0.19	$-0.84^{+0.02}_{-0.02}$	—	108 (85)	0.049
	SMC/po	$1.53^{+0.28}_{-0.26}$	<0.18	$-0.84^{+0.02}_{-0.02}$	—	108 (85)	0.050
	MW/bknpo	$1.53^{+0.28}_{-0.26}$	$0.07^{+0.07}_{-0.07}$	$-0.84^{+0.02}_{-0.02}$	*	107 (84)	0.043
	LMC/bknpo	$1.53^{+0.28}_{-0.26}$	<0.19	$-0.84^{+0.02}_{-0.02}$	*	108 (84)	0.042
	SMC/bknpo	$1.53^{+0.28}_{-0.26}$	<0.18	$-0.84^{+0.02}_{-0.02}$	*	108 (84)	0.043
130603B	MW/po	$2.43^{+0.24}_{-0.22}$	$0.79^{+0.05}_{-0.05}$	$-0.83^{+0.01}_{-0.01}$	—	58 (50)	0.206
	LMC/po	$2.42^{+0.24}_{-0.22}$	$0.76^{+0.05}_{-0.05}$	$-0.82^{+0.01}_{-0.01}$	—	57 (50)	0.218
	SMC/po	$2.39^{+0.24}_{-0.22}$	$0.72^{+0.05}_{-0.05}$	$-0.82^{+0.01}_{-0.01}$	—	56 (50)	0.253
	MW/bknpo	$2.99^{+0.30}_{-0.36}$	$1.14^{+0.10}_{-0.10}$	$-0.98^{+0.08}_{-0.07}$	8^{+19}_{-6}	48 (49)	0.498
	LMC/bknpo	$3.01^{+0.38}_{-0.36}$	$1.09^{+0.09}_{-0.09}$	$-0.98^{+0.08}_{-0.07}$	8^{+21}_{-6}	48 (49)	0.505
	SMC/bknpo	$3.10^{+0.42}_{-0.20}$	$0.99^{+0.09}_{-0.09}$	$-1.00^{+0.08}_{-0.07}$	15^{+38}_{-11}	49 (49)	0.477
140903A	MW/po	$1.53^{+0.31}_{-0.28}$	$0.79^{+0.23}_{-0.24}$	$-0.80^{+0.03}_{-0.03}$	—	49 (39)	0.128
	LMC/po	$1.53^{+0.31}_{-0.28}$	$0.76^{+0.22}_{-0.23}$	$-0.80^{+0.03}_{-0.03}$	—	49 (39)	0.130
	SMC/po	$1.51^{+0.30}_{-0.27}$	$0.74^{+0.21}_{-0.22}$	$-0.79^{+0.03}_{-0.03}$	—	49 (39)	0.139
	MW/bknpo	$1.53^{+0.31}_{-0.28}$	$0.79^{+0.23}_{-0.24}$	$-0.80^{+0.03}_{-0.03}$	*	49 (38)	0.106
	LMC/bknpo	$1.53^{+0.31}_{-0.28}$	$0.76^{+0.22}_{-0.23}$	$-0.80^{+0.03}_{-0.03}$	*	49 (38)	0.108
	SMC/bknpo	$1.51^{+0.30}_{-0.27}$	$0.74^{+0.21}_{-0.21}$	$-0.79^{+0.03}_{-0.03}$	*	49 (38)	0.116
150423A	MW/po	$1.59^{+1.50}_{-1.17}$	<0.55	$-0.76^{+0.03}_{-0.03}$	—	6 (7)	0.536
	LMC/po	$1.59^{+1.50}_{-1.17}$	<0.57	$-0.76^{+0.03}_{-0.03}$	—	6 (7)	0.536
	SMC/po	$1.59^{+1.50}_{-1.17}$	<0.56	$-0.76^{+0.03}_{-0.03}$	—	6 (7)	0.536
	MW/bknpo	$1.59^{+1.50}_{-1.17}$	<0.55	$-0.76^{+0.03}_{-0.03}$	*	6 (6)	0.419
	LMC/bknpo	$1.59^{+1.50}_{-1.17}$	<0.57	$-0.76^{-0.50}_{-0.50}$	*	6 (6)	0.419
	SMC/bknpo	$1.59^{+1.50}_{-1.17}$	<0.56	$-0.76^{+0.03}_{-0.03}$	*	6 (6)	0.419
150424A	MW/po	<0.09	<0.03	$-0.76^{+0.01}_{-0.01}$	—	89 (47)	2.66e-02
	LMC/po	<0.09	<0.03	$-0.76^{+0.01}_{-0.01}$	—	89 (47)	2.66e-02
	SMC/po	<0.09	<0.03	$-0.76^{+0.01}_{-0.01}$	—	89 (47)	2.66e-02
	MW/bknpo	$0.32^{+0.23}_{-0.22}$	<0.15	$-1.01^{+0.06}_{-0.06}$	59^{+82}_{-34}	66 (46)	0.027
	LMC/bknpo	$0.32^{+0.23}_{-0.22}$	<0.16	$-1.01^{+0.06}_{-0.06}$	59^{+82}_{-34}	66 (46)	0.027
	SMC/bknpo	$0.32^{+0.23}_{-0.22}$	<0.15	$-1.01^{+0.06}_{-0.06}$	59^{+82}_{-34}	66 (46)	0.027
170428A	MW/po	<2.55	<0.09	$-0.73^{+0.03}_{-0.02}$	—	8 (7)	0.344
	LMC/po	<2.55	<0.06	$-0.73^{+0.03}_{-0.02}$	—	8 (7)	0.344
	SMC/po	<2.55	<0.06	$-0.73^{+0.03}_{-0.02}$	—	8 (7)	0.344
	MW/bknpo	<3.72	<0.28	$-0.92^{+0.16}_{-0.17}$	26^{+238}_{-23}	2 (6)	0.870
	LMC/bknpo	<3.72	<0.22	$-0.91^{+0.17}_{-0.15}$	20^{+247}_{-18}	3 (6)	0.869
	SMC/bknpo	<3.72	<0.21	$-0.92^{+0.16}_{-0.17}$	26^{+238}_{-23}	2 (6)	0.870

* Break energy is restricted by the lower limit we set.

References

Abbott, B. P., et al. 2017, ApJ, 848, L12

Belczynski, K., Perna, R., Bulik, T., Kalogera, V., Ivanova, N., & Lamb, D. Q. 2006, ApJ, 648, 1110

Berger, E. 2014, ARA&A, 52, 43

Berger, E., et al. 2005, Nature, 438, 988

Berger, E., Cenko, S. B., Fox, D. B., & Cucchiara, A. 2009, ApJ, 704, 877

Bloom, J. S, Kulkarni, S. R., & Djorgovski, S. G. 2002, AJ, 123, 1111

Bloom, J. S, Sigurdsson, S., & Pols, O. 1999, MNRAS, 305, 763

Bolmer, J., Steinle, H., & Schady, P. 2017, GCN Circ., 21050

Burrows, D., et al. 2005, Space Sci. Rev., 120, 165

Ciotti, L., & Bertin, G. 1999, A&A, 352, 447

Covino, S., et al. 2013, MNRAS, 432, 1231

de Ugarte Postigo, A., et al. 2014, A&A, 563, A62

Eichler, D., Livio, M., Piran, T., & Schramm, D. N. 1989, Nature, 340, 126
Evans, P. A., et al. 2007, A&A, 469, 379
Evans, P. A., et al. 2009, MNRAS, 397, 1177
Fong, W., et al. 2013, ApJ, 769, 56
Fong, W., & Berger, E. 2013, ApJ, 776, 18
Fong, W., Berger, E., Margutti, R., & Zauderer, B. A. 2015, ApJ, 815, 102
Fruchter, A. S, et al. 2006, Nature, 441, 463
Fryer, C. L., Woosley, S. E., & Hartmann, D. H. 1999, ApJ, 526, 152
Galama, T. J., & Wijers, R. A. M. J. 2001, ApJ, 549, L209
Gehrels, N., et al. 2004, ApJ, 611, 1005
Goldstein, A., et al. 2017, ApJ, 848, L14
Granot, J., & Sari, R. 2002, ApJ, 568, 820
Hjorth, J., et al. 2003, Nature, 423, 847
Kagawa, Y., Yonetoku, D., Sawano, T., Toyanago, A., Nakamura, T., Takahashi, K., Kashiyama, K., & Ioka, K. 2015, ApJ, 811, 4
Kann, D. A., Kruehler, T., Klose, S., & Greiner, J. 2015, GCN Circ., 1, 17738
Kisaka, S., Ioka, K., & Sakamoto, T. 2017, ApJ, 846, 142
Knust, F., et al. 2017, A&A, 607, A84
Kouveliotou, C., Meegan, C. A., Fishman, G. J., Bhat, N. P., Briggs, M. S., Koshut, T. M., Paciesas, W. S., & Pendleton, G. N. 1993, ApJ, 413, L101
Krühler, T., et al. 2011, A&A, 534, A108
Kumar, P., & Zhang, B. 2015, Phys. Rep., 561, 1
Levan, A. J., et al. 2017, ApJ, 848, L28
Lien, A., et al. 2016, ApJ, 829, 7
Littlejohns, O., et al. 2015, GCN Circ., 17736
Malesani, D., et al. 2007, A&A, 473, 77
Narayan, R., Paczynski, B., & Piran, T. 1992, ApJ, 395, L83
Nicuesa Guelbenzu, A., et al. 2012, A&A, 538, L7
Norris, J. P., & Bonnell, J. T. 2006, ApJ, 643, 266
Pei, Y. C. 1992, ApJ, 395, 130
Pooley, D., Kumar, P., Wheeler, J.C., & Grossan, B. 2018, ApJ, 859, L23
Rees, M. J., & Mészáros, P. 1992, MNRAS, 258, 41P
Rees, M. J., & Mészáros, P. 1998, ApJ, 496, L1
Sari, R., Piran, T., & Narayan, R. 1998, ApJ, 497, L17
Savaglio, S., Fall, S. M., & Fiore, F. 2003, ApJ, 585, 638
Savchenko, V., et al. 2017, ApJ, 848, L15
Schady, P., et al. 2007, MNRAS, 377, 273
Schady, P., et al. 2010, MNRAS, 401, 2773
Schlafly, E. F., & Finkbeiner, D. P. 2011, ApJ, 737, 103
Soderberg, A. M., et al. 2006, ApJ, 650, 261
Svensson, K. M., Levan, A. J., Tanvir, N. R., Fruchter, A. S., & Strolger, L.-G. 2010, MNRAS, 405, 57
Troja, E., et al. 2016, ApJ, 827, 102
Troja, E., et al. 2017, GCN Circ., 21051
Varela, K., Knust, F., & Greiner, J. 2015, GCN, 1, 17732
Waxman, E., & Draine, B. T. 2000, ApJ, 537, 796
Welty, D. E., Xue, R., & Wong, T. 2012, ApJ, 745, 173
Willingale, R., Starling, R. L. C., Beardmore, A. P., Tanvir, N. R., & O'Brien, P. T. 2013, MNRAS, 431, 394
Woosley, S. E., & Bloom, J. S. 2006, ARA&A, 44, 507
Zafar, T., Watson, D., Fynbo, J. P. U., Malesani, D., Jakobsson, P., & de Ugarte Postigo, A. 2011, A&A, 532, A143